Surface charge measurements on different dielectrics in diffuse and filamentary barrier discharges

OPEN ACCESS
IOP Publishing
Journal of Physics D: Applied Physics
J. Phys. D: Appl. Phys. **50** (2017) 105207 (13pp)
doi:10.1088/1361-6463/aa5605

Surface charge measurements on different dielectrics in diffuse and filamentary barrier discharges

R Tschiersch[1], S Nemschokmichal[1], M Bogaczyk[2] and J Meichsner[1]

[1] Institute of Physics, University of Greifswald, Felix-Hausdorff-Str. 6, 17489 Greifswald, Germany
[2] Leibniz Institute for Plasma Science and Technology, Felix-Hausdorff-Str. 2, 17489 Greifswald, Germany

E-mail: robert.tschiersch@uni-greifswald.de

Received 8 November 2016
Accepted for publication 29 December 2016
Published 10 February 2017

Abstract

Previously, we reported on the measurement of surface charges during the operation of barrier discharges (BDs) using the electro-optic Pockels effect of a bismuth silicon oxide (BSO) crystal. With the present work, the next milestone is achieved by making this powerful method accessible to various dielectrics which are typically used in BD configurations. The dynamics and spatial distribution of positive and negative surface charges were determined on optically transparent borosilicate glass, mono-crystalline alumina and magnesia, respectively, covering the BSO crystal. By variation of the nitrogen admixture to helium and the pressure between 500 mbar and 1 bar, both the diffuse glow-like BD and the self-stabilized discharge filaments were operated inside of a gas gap of 3 mm. The characteristics of the discharge and, especially, the influence of the different dielectrics on its development were studied by surface charge diagnostics, electrical measurements and ICCD camera imaging. Regarding the glow-like BD, the breakdown voltage changes significantly by variation of the cathodic dielectric, due to the different effective secondary electron emission (SEE) coefficients. These material-specific SEE yields were estimated using Townsend's criterion in combination with analytical calculations of the effective ionization coefficient in helium with air impurities. Moreover, the importance of the surface charge memory effect for the self-stabilization of discharge filaments was quantified by the recalculated spatio-temporal behavior of the gap voltage.

Keywords: barrier discharge, surface charge, memory effect, gap voltage, secondary electron emission coefficient, borosilicate, alumina, magnesia

(Some figures may appear in colour only in the online journal)

1. Introduction

The most characteristic feature of barrier discharges (BDs) consists in the deposition of charge carriers from the discharge volume onto the surface of the dielectric-covered electrodes. During the discharge breakdown, these so-called surface charges cause an electric field that is oppositely directed to the external electric field, wherefore the current is limited and, finally, the discharge extinguishes. As a result, BDs generate non-equilibrium plasmas at elevated pressures, serving as an effective source of high-energy electrons, photons, radicals and excited species [1, 2]. The high chemical reactivity at low gas temperature and comparatively low power consumption, as well as the possibility to operate without expensive vacuum equipment, make the BD indispensable for numerous industrial applications [3, 4], e.g. surface treatment and modification of heat-sensitive materials in biology and medicine.

The spatial distribution and the dynamic behavior of surface charges significantly determine the fundamental mechanisms of diffuse and filamentary BDs. As a prominent

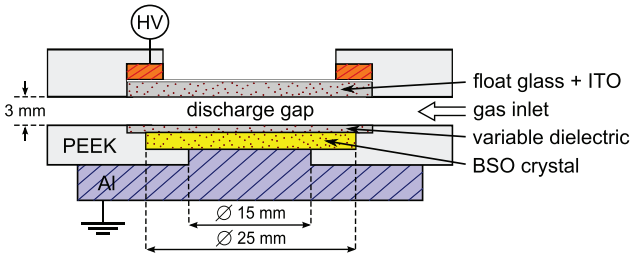

Figure 1. Sketch of the discharge configuration from side-view. The dielectric plate on top of the BSO crystal was varied to consist of borosilicate glass, alumina, and magnesia, respectively.

example, the periodic discharge re-ignition is favored by the electric field enhancement, due to residual surface charges on the dielectrics, which is well-known as the surface memory effect [5, 6]. That is why the current filaments of microdischarges in plane-parallel electrode configurations can reignite at the same lateral positions for several discharge cycles [7, 8], and the self-organized pattern of BDs in a lateral direction is conserved [9, 10]. Indeed, the lifetime of surface charges from the sub-second up to the minute time scale clearly exceeds the typical discharge off-time [8, 11].

Up to now, experimental proof of the physical nature of surface charges is still missing, but an accepted hypothesis exists. Negative surface charges are electrons adsorbed onto the dielectric surface, with low material-dependent binding energy in the order of 1 eV [12–14]. Theoretical calculations reveal that these electrons are either trapped in shallow image potential states just in front of the crystallographic boundary, or in the conduction band just inside the dielectric, which depends on the material-specific electron affinity [15]. However, positive surface charges are assumed to be defect electrons (positive holes) generated by ion-electron recombination at the dielectric surface. Hence, besides the electrostatic effect of the surface charges, the weakly bound surface electrons may act as an important seed electron reservoir that supports the pre-ionization. Especially, thermal desorption of surface electrons may favor the formation of diffuse BDs driven by a low operating frequency in helium and oxygen-containing systems. Here, metastable states do not survive during the discharge off-time and thus can not contribute to the pre-ionization by Penning ionization and secondary electron emission [12, 16, 17].

From an experimental point of view, the fundamental knowledge about the role of surface charges in BDs was mainly obtained using the electro-optic Pockels effect of a bismuth silicon oxide (BSO) crystal [7–11]. Although this method is already well-established, up to now it has been restricted to the specific BSO crystal exposed to the discharge. The present paper reports on the extension of this diagnostic technique to more common dielectric materials, such as borosilicate glass, alumina and magnesia. The investigations are focused on the influence of these dielectrics on the development of diffuse and filamentary BDs characterized by electrical quantities, the optical emission, as well as the spatial distribution and dynamics of surface charges.

The outline of this paper is as follows. Section 2 briefly describes the experiment and the principles of the methodology. Section 3 presents the surface charge measurements for the operation of the glow-like BD, including the estimation of effective SEE coefficients for the different dielectric materials using Townsend's criterion. Finally, the surface charge memory effect on the conservation of the lateral structure of multiple and single discharge filaments is discussed in section 4.

Table 1. Composition, thickness d, and permittivity ε_r of the dielectric materials installed in the discharge configuration.

Dielectric material	Composition	d (mm)	ε_r
Float glass (+ITO layer)	unspecified	0.70(5)	7.6
Borosilicate glass	~80% SiO_2 ~12% B_2O_3 ~8% Na_2O	0.21(1)	6.7
Mono-crystalline alumina	Al_2O_3	0.20(1)	10.6
Mono-crystalline magnesia	MgO	0.20(1)	9.7
Bismuth silicon oxide crystal	$Bi_{12}SiO_{20}$	0.70(5)	56

2. Experimental setup and methodology

2.1. Discharge configuration

The discharge cell is depicted from the side-view in figure 1. The plane-parallel electrode configuration is shielded with dielectrics on both sides to the discharge in a 3 mm gas gap. The upper high-voltage driven electrode is a copper ring connected to an electrically conductive and optically transparent ITO layer on top of a float glass plate. A bismuth silicon oxide (BSO) crystal is placed on a grounded aluminum mirror and covered with a thin optically transparent dielectric plate. The latter was varied to consist of borosilicate glass, mono-crystalline alumina and magnesia, respectively. This setup allows the measurement of surface charges on top of the different dielectrics via the electro-optic Pockels effect of the BSO crystal. Some properties of the used dielectric materials are summarized in table 1.

2.2. Vacuum system and gas supply

The discharge cell is placed inside a vacuum chamber made of stainless steel. Before the operating gas is passed directly into the discharge volume, the chamber is pumped to a base pressure below 10^{-5} mbar. Two mass flow controllers set the gas flow rate of helium and nitrogen (respective purity >99.999%) to realize well-defined He/N_2 mixtures. The operating pressure amounts to 500 mbar or 1 bar, and is kept constant in the flowing regime (100 sccm) by a diaphragm pressure gauge (MKS) in combination with a butterfly valve (MKS) and a process pump (TRIVAC D25BCSPFPE).

2.3. Electrical measurements

Figure 2 illustrates the entire diagnostic setup which enables the simultaneous investigation of (a) electrical discharge quantities, (b) the surface charge dynamics and (c) the optical emission from the discharge volume.

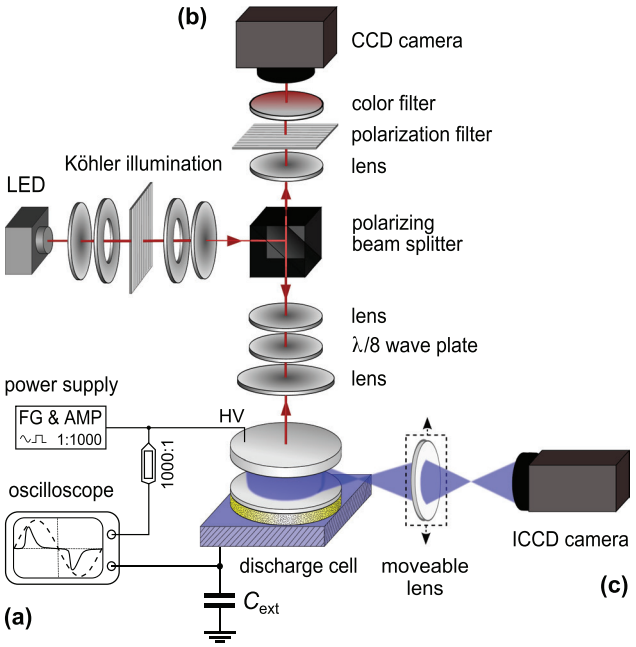

Figure 2. Experimental setup: (a) measurement of applied voltage and total charge, (b) surface charge diagnostics via the electro-optic Pockels effect and (c) measurement of the optical emission from the discharge by ICCD camera imaging. Further details are given in the text.

The sine- or square-wave feeding voltage $U_{ext}(t)$ at the frequency of 2 kHz is provided by a function generator (SRS DS345) in combination with an amplifier (Trek 615-10, 1:1000), measured via a HV probe and connected to the upper electrode. The total transported charge $Q_{ext}(t)$ is detected by an external capacitor ($C_{ext} = 1.2$ nF) at the grounded electrode. The voltage signals are monitored and averaged by a digital oscilloscope (ROHDE&SCHWARZ RTO1024) with a bandwidth of 2 GHz. Based on the equivalent circuit in figure 3 according to [18], internal electrical quantities of the diffuse discharge can be recalculated, such as the voltage drop across the gas gap

$$U_{gap}(t) = \left(1 + \frac{C_{par}}{C_{die}}\right)U_{ext}(t) - \frac{1}{C_{die}}Q_{ext}(t), \qquad (1)$$

the discharge current without any displacement current

$$I_{dis}(t) = \left(1 + \frac{C_{gap}}{C_{die}}\right)\left(\frac{dQ_{ext}(t)}{dt} - C_{tot}\frac{dU_{ext}(t)}{dt}\right), \qquad (2)$$

and the time-integral of the discharge current, which describes the accumulation of surface charges

$$Q_{sur}(t) = \left(1 + \frac{C_{gap}}{C_{die}}\right)(Q_{ext}(t) - C_{tot}\,U_{ext}(t)). \qquad (3)$$

Here, the capacitances C_{die} and C_{gap} of the dielectrics and the discharge gap, respectively, are calculated by considering the cell geometry and the dielectric properties in table 1. Moreover, C_{tot} is the total capacitance derived from the $Q_{ext}(U_{ext})$ plot (Lissajous-figure), and the capacitance $C_{par} = C_{tot} - C_{gap}C_{die}/(C_{gap} + C_{die})$ considers the surrounding region beyond the lateral discharge extent.

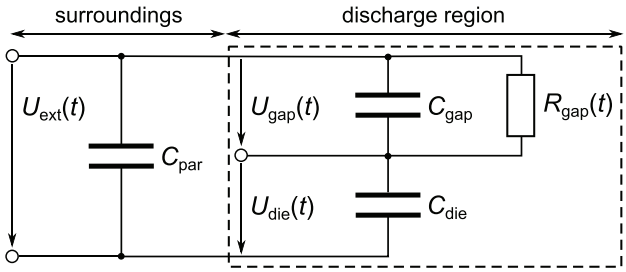

Figure 3. Electrical equivalent circuit: the discharge gap is represented by the time-dependent resistance $R_{gap}(t)$ connected in parallel with the capacitance C_{gap}. All dielectrics connected in series determine the capacitance C_{die}, and C_{par} considers the parallel capacitance beyond the lateral discharge extent.

2.4. Surface charge diagnostics

The surface charge diagnostics is based on the electro-optic Pockels effect of the BSO crystal [7]. Figure 2(b) shows the optical setup. The LED light ($\lambda = 634$ nm) is homogenized by passing the Köhler illumination, before it is diverted into the direction of the discharge configuration by means of a linearly polarizing beam splitter. Following this path, the LED light becomes elliptically polarized by a $\lambda/8$ wave plate, expanded by a telescopic system and passes the discharge cell twice, due to reflection at the grounded aluminum mirror. On the way back, the LED light passes a color filter which blocks the radiation from the discharge, and a second polarization filter allowing the light intensity to be measured by a CCD camera (Miro 4ex, minimal exposure time of 2 μs). During the discharge operation, the voltage drop U_{BSO} across the BSO crystal, caused by both the deposited surface charges (U^{σ}_{BSO}) and the applied voltage (U^{ext}_{BSO}), induces a birefringence and thus an additional change in the polarization of the LED light according to the phase difference

$$\Delta\Phi(U_{BSO}) = \frac{2\pi}{\lambda}n_0^3 r_{41}U_{BSO} = k(U^{\sigma}_{BSO} + U^{ext}_{BSO}). \qquad (4)$$

The proportionality factor k, including the wavelength λ of the LED light, and the refraction index n_0 and Pockels coefficient r_{41} of the BSO crystal, is experimentally determined from a calibration procedure. Further details and corresponding analytical calculations are given in [7]. Covering the BSO crystal with a variable transparent dielectric plate is the innovative feature of the present paper, as depicted in figure 4. As a result, the surface charge is deposited and measured on this thin dielectric plate. Therefore, the surface charge density σ_{sur} causes the total voltage drop U^{σ} across both the variable dielectric X and the BSO crystal, wherein both can be treated as ideal capacitors with thickness d_X and d_{BSO}, and permittivity ε_X and ε_{BSO},

$$U^{\sigma} = U^{\sigma}_{X} + U^{\sigma}_{BSO} = \frac{d_X\sigma_{sur}}{\varepsilon_0\varepsilon_X} + \frac{d_{BSO}\sigma_{sur}}{\varepsilon_0\varepsilon_{BSO}}. \qquad (5)$$

Hence, covering the BSO crystal with another dielectric leads to an increase of the total voltage drop U^{σ} by U^{σ}_{X} at an otherwise constant surface charge density, since the effective capacitance is reduced. But, only the voltage drop U^{σ}_{BSO} across the BSO crystal contributes to the electro-optic

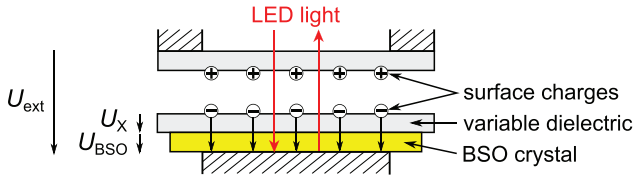

Figure 4. Principle of surface charge diagnostics: by passing the BSO crystal, the polarization of the LED light changes due to the electro-optic Pockels effect, which is particularly induced by the deposited charges on the surface of the variable dielectric.

change in the polarization of the LED light, according to equation (4). Thus, the spatio-temporally resolved surface charge density

$$\sigma_{sur}(x,y,t) = \frac{\varepsilon_0 \varepsilon_{BSO}}{d_{BSO}}\left(\frac{I_{meas}}{I_{ref}} - 1\right)\left(U^{ext}_{BSO} + \frac{1}{2k}\right) \qquad (6)$$

is calculated using the same formula as for the mere BSO crystal without a further dielectric on top [7]. In equation (6), $I_{meas}(U^{ext}_{BSO} + U^{\sigma}_{BSO})$ is the measured light intensity during the discharge operation, and $I_{ref}(U^{ext}_{BSO})$ denotes the reference intensity without any discharge and thus dependent on the applied voltage, but independent of surface charges.

Moreover, for the first time, the spatio-temporal evolution of the gap voltage

$$U_{gap}(x,y,t) = \frac{C^{px}_{die}}{C^{px}_{die} + C^{px}_{gap}} U_{ext}(t) - \frac{A^{px}}{C^{px}_{die}}\,\sigma_{sur}(x,y,t), \qquad (7)$$

is calculated from the measured surface charge density distribution $\sigma_{sur}(x,y,t)$ for the filamentary discharge mode. Here, $A^{px} = 4 \times 10^{-5}\,\mathrm{cm}^2$ means the observation area detected per pixel of the CCD camera chip.

2.5. ICCD camera imaging

The optical emission from the discharge volume is detected by a gated intensified charge-coupled device (ICCD) camera (Princeton Instruments PI-MAX). The camera chip (512 × 512 pixel and 0.12 mm/pixel spatial resolution), combined with the 1:-3 imaging of the discharge volume via an external lens, provides an effective spatial resolution of 0.04 mm in the axial as well as lateral direction. In particular, the temporal resolution down to 1 ns allows us to follow the fast two-dimensional development of the filamentary discharge.

3. Diffuse glow-like discharge

3.1. Surface charge accumulation and dynamics

A laterally homogeneous discharge with one breakdown per half-cycle of the sine-wave voltage ($\hat{U}_{ext} = 0.8$ kV) was operated in pure helium (purity >99.999%) at a pressure of 500 mbar, at first, with borosilicate glass on top of the BSO crystal. In figure 5, the applied voltage $U_{ext}(t)$, the gap voltage $U_{gap}(t)$ and the discharge current $I_{dis}(t)$ are plotted for one discharge cycle. Also, the ICCD images of the discharge volume from the side-view as well as the surface charge density distribution on the bottom dielectric are shown for different

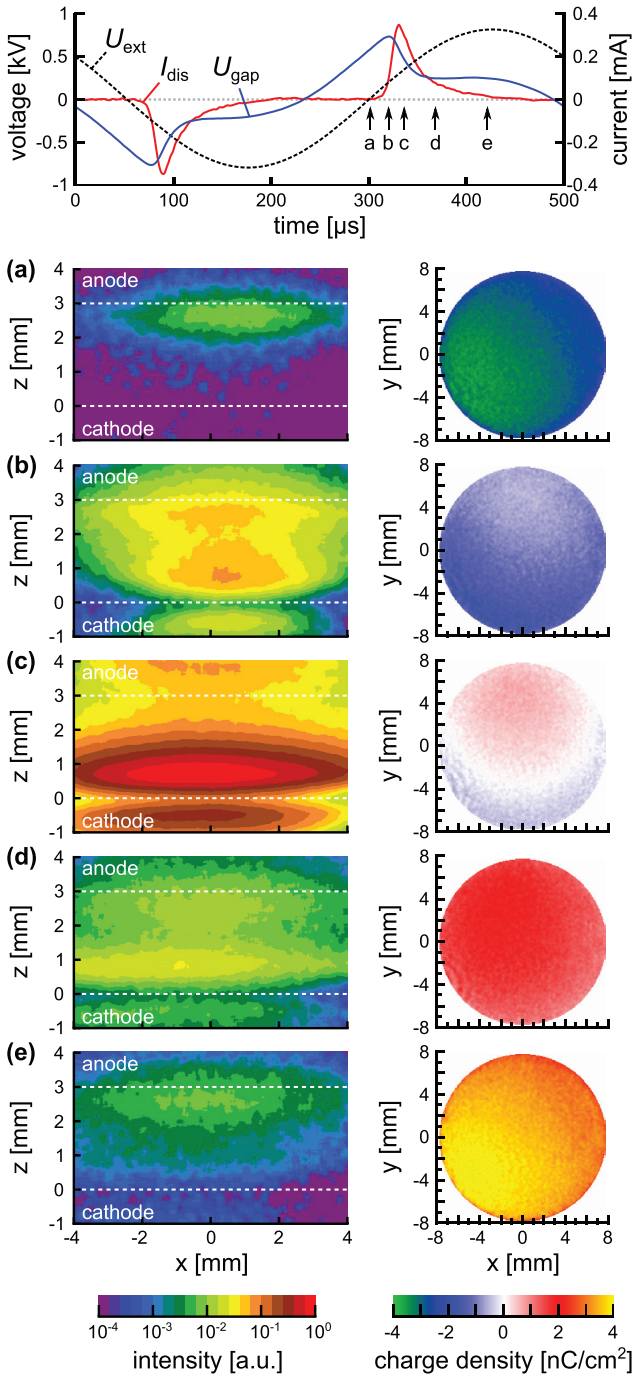

Figure 5. Development of the diffuse glow-like BD in nominally pure helium: applied voltage $U_{ext}(t)$, gap voltage $U_{gap}(t)$ and discharge current $I_{dis}(t)$ for one discharge cycle (above), and ICCD camera images of the optical discharge emission from the side-view as well as surface charge density distribution on the bottom dielectric at different times (a)–(e) during the positive discharge breakdown (below). Borosilicate glass on top of the BSO crystal, $p = 500$ mbar, $\hat{U}_{ext} = 0.8$ kV.

times (a)–(e) during the discharge pulse within the positive half-cycle. The discharge current peaks at ±0.4 mA with a pulse duration of about 100 µs. Note that there is no remarkable asymmetry comparing the two half-cycles of the feeding voltage, which indicates similar properties (permittivity, SEE coefficients) of the upper and lower dielectric. During the discharge breakdown, the drop in gap voltage is significantly

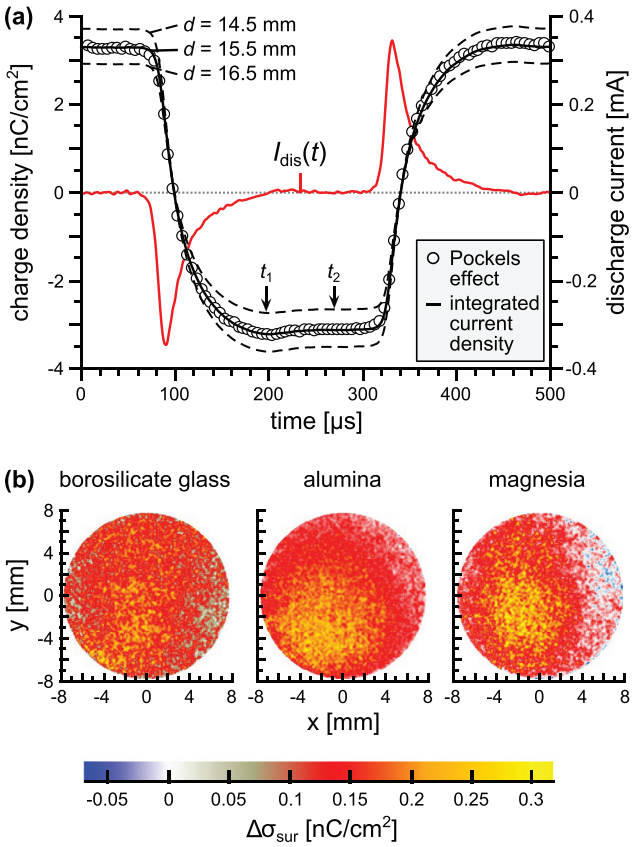

Figure 6. (a) Comparison of phase-resolved transported charge and deposited surface charge for the diffuse glow-like BD in nominally pure helium. The circles represent the surface charge density determined using the electro-optic Pockels effect. The solid and dashed black lines represent the charge density, which is calculated by the time-integral of the measured discharge current $I_{dis}(t)$ divided by the circular discharge area for three different diameters. Borosilicate glass on top of the BSO crystal, $p = 500$ mbar, $\hat{U}_{ext} = 0.8$ kV. (b) Difference in spatially resolved surface charge density $\Delta\sigma_{sur} = \sigma_{sur}(t_2) - \sigma_{sur}(t_1)$ between t_2 and t_1 indicated in (a) for the different highlighted dielectrics.

large, which is typical for the glow-like barrier discharge in helium for gas gap widths larger than 1 mm [5, 19].

Indeed, the ICCD camera images of the optical emission reveal a Townsend pre-phase indicated by the weak emission maximum in front of the anode (a), followed by a cathode-directed light emission (b) with intensive negative glow when the maximum discharge current is reached (c), fading away during the afterglow (d) and ending up in a residual emission maximum in front of the anode (e). The associated surface charge density distributions reveal that the discharge does not ignite simultaneously over the entire electrode area, but starts within the top-right sector and ends in the opposite one. Taking a closer look, this is confirmed from the side-view by the ICCD camera images too. This discharge inhomogeneity might be caused by lateral deviations in the inter-electrode distance and thus in the gap voltage, and by an inhomogeneous gas flow, which results in uncertainties of the gas impurity (M) concentration. The gas impurities in helium determine the total ionization rate by Penning ionization

$$\mathrm{M} + \mathrm{He^m/He_2^m} \rightarrow \mathrm{M^+} + \mathrm{e^-} + \mathrm{He/2He} \qquad (8)$$

during the pre-phase and the breakdown [17, 19, 20]. Here, $\mathrm{He^m}$ and $\mathrm{He_2^m}$ denote the metastable helium atoms and molecules, respectively. Consequently, the breakdown voltage must be higher in regions with a lower impurity level, resulting in a more intensive discharge.

In figure 6(a), the phase-resolved surface charge density, determined via the electro-optic Pockels effect and averaged over the observation area, is plotted for one discharge cycle and compared with the charge density Q_{sur}/A_{dis} that is recalculated from the measured electrical quantities according to equation (3) using different diameters d of the circular discharge area $A_{dis} = \pi d^2/4$. Very good qualitative and quantitative agreement is achieved for a discharge diameter of 15.5 mm that is close to the diameter of the grounded electrode (15 mm). The latter defines the observation area of the surface charge diagnostics. This result validates the applicability of this method to other transparent dielectrics covering the BSO crystal, and it exceeds the accuracy of previous studies [7, 8].

It is also conspicuous in figure 6(a) that the surface charge density slightly decreases between the times t_1 and t_2 after the discharge breakdown in the negative half-cycle, when surface electrons have been adsorbed onto the bottom dielectric. The corresponding change in surface charge density distribution $\Delta\sigma_{sur}$ is shown in figure 6(b) for the different dielectrics studied. Note that $\Delta\sigma_{sur}$ is largest in the bottom-left sector where the surface charge density is highest. In fact, one cannot exclude surface electron transport into the outer regions, due to lateral gradients in the charge density. However, $\Delta\sigma_{sur}$ has the same sign over the entire discharge area. As indicated by the gap voltage in figure 5, there might be a region of low electric field during the discharge afterglow. Thus, most likely, the decrease in negative surface charge density after the breakdown is the result of the recombination of ions stored in the positive column with electrons trapped in the image potential just in front of the anodic dielectric [15].

3.2. *Influence of different dielectrics*

In the following, the influence of the dielectric material on the electrical characteristics of the diffuse glow-like BD in nominally pure helium at 500 mbar is discussed. In figure 7(a), the applied voltage $U_{ext}(t)$, (b) the gap voltage $U_{gap}(t)$, (c) the discharge current $I_{dis}(t)$ and (d) the surface charge density $\sigma_{sur}(t)$ are plotted for one discharge cycle using borosilicate glass, alumina and magnesia on top of the BSO crystal, respectively. In each case, the sine-wave feeding voltage has the same amplitude $\hat{U}_{ext} = 0.8$ kV and triggers the recording of all other quantities. Based on the zero-crossing of the calculated gap voltage, the entire discharge cycle can be subdivided into two sections: the variable dielectric X is the anodic dielectric or the cathodic dielectric.

If the variable dielectric is the anodic one, there is no significant mismatch comparing the gap voltage and the discharge current for the three dielectrics. But one should keep in mind that the current amplitude is slightly larger for alumina. In contrast, if the variable dielectric is the cathodic one, the voltage required for discharge breakdown is clearly highest for borosilicate glass and lowest for magnesia (ΔU_{gap}). Moreover,

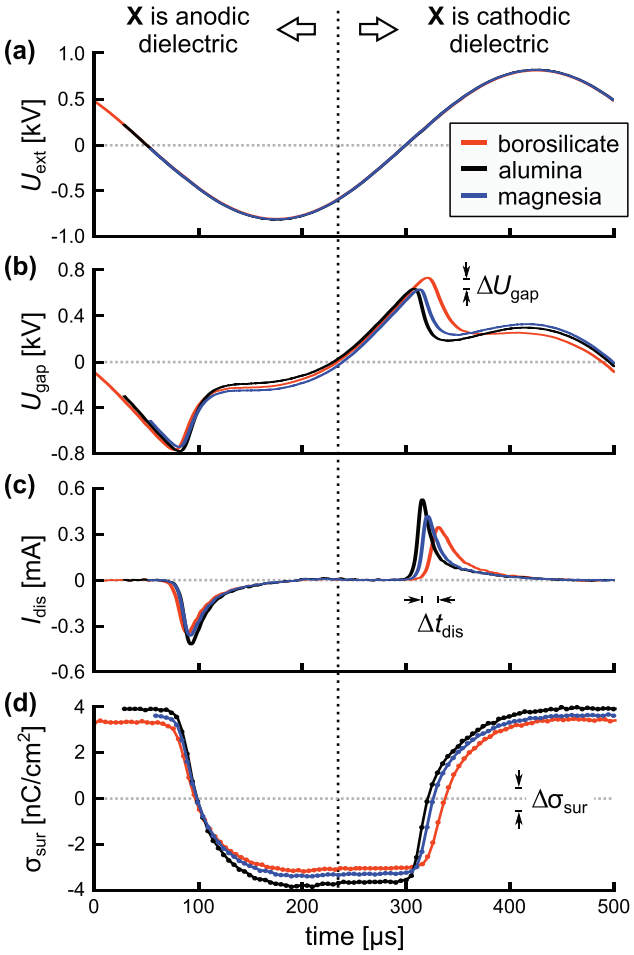

Figure 7. Influence of borosilicate glass, alumina and magnesia on the development of the diffuse glow-like BD: (a) applied voltage $U_{ext}(t)$, (b) gap voltage $U_{gap}(t)$, (c) discharge current $I_{dis}(t)$ and (d) spatially averaged surface charge density $\sigma_{sur}(t)$. The zero-crossing of the gap voltage marks the transition for the respective material to be the anodic dielectric or the cathodic dielectric. Nominally pure He, $p = 500$ mbar, $\hat{U}_{ext} = 0.8$ kV.

the discrepancy in the breakdown voltage corresponds to a delay in the breakdown onset (Δt_{dis}) with respect to the feeding voltage. The transported and subsequently deposited charge density is smallest for borosilicate glass, closely followed by magnesia, and clearly largest for alumina ($\Delta\sigma_{sur}$). Since the residual surface charge acts as a memory between the consecutive discharge breakdowns, the transported charge is again largest for alumina during the current pulse in the negative half-cycle, as already mentioned.

Indeed, there is a crucial difference in acting as the anodic dielectric and the cathodic dielectric. During the pre-phase, the anodic dielectric has a passive role for the discharge development, because it is charged with positive holes resulting from the recombination of incident ions with electrons from the dielectric surface during the previous breakdown [12]. However, the cathodic dielectric is charged with residual surface electrons in shallow traps in the order of 1 eV [12, 21]. These weakly bound surface electrons are thus easier to release than the electrons from the valence band. Since the actual binding energy of surface electrons is specific of the

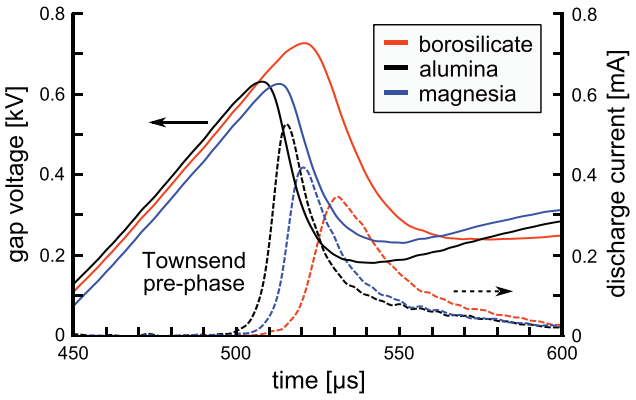

Figure 8. Influence of different cathodic dielectrics on the diffuse discharge breakdown within the positive half-cycle of the feeding voltage. For each dielectric, the gap voltage $U_{gap}(t)$ and the discharge current $I_{dis}(t)$ are plotted by a solid line and a dashed line, respectively. Pure He, $p = 500$ mbar, $\hat{U}_{ext} = 0.8$ kV.

respective dielectric material, the secondary electron emission (SEE) yield differs as well. Hence, the active role of the cathodic dielectric due to both ordinary SEE from the valance band as well as additional SEE from the shallow traps causes the mismatch in breakdown voltage when comparing the three dielectrics in figure 7(b). The breakdown voltage decreases with increasing SEE yield, which is thus largest for magnesia, followed by alumina and smallest for borosilicate glass.

At otherwise constant discharge conditions, the changing effective SEE yield is linked to the differing properties of the dielectrics, e.g. binding energy of intrinsic electrons [22], trapping mechanisms, binding energy, and amount of surface electrons [13, 15, 23, 24] and surface roughness [25]. The energy gap between the conduction band and the valance band filled with intrinsic electrons is largest for silica and smallest for magnesia [22]. Following the model in [15], electrons hitting the surface of magnesia are trapped in image-potential states just in front of the crystallographic boundary, whereas in the case of silica and alumina, incident electrons populate the conduction band (with subsequent energy relaxation). Moreover, the energy of the incoming projectile, such as ions, metastable species or photons, is crucial since the resonant charge transfer at the dielectric surface is preferred [22]. Also, the effective SEE yield depends on the surface charge amount that increases with rising permittivity [24]. The latter is largest for alumina ($\varepsilon_r = 10.55$), closely followed by magnesia ($\varepsilon_r = 9.65$) and clearly smallest for borosilicate glass ($\varepsilon_r = 6.7$).

3.3. Estimation of effective SEE coefficients

Figure 8 zooms into the positive half-cycle of figures 7(b) and (c). At this time, the varied dielectric is the cathodic one, which therefore directly influences the discharge development by SEE. The maximum gap voltage defines the breakdown voltage U_b. The latter is used to estimate the effective SEE coefficient for the different dielectrics based on Townsend's criterion

$$\gamma_{eff}(U_b) = \left[\exp\left(\int_0^g \alpha_{eff}(E/n(z))\mathrm{d}z\right) - 1\right]^{-1}, \qquad (9)$$

Table 2. Elementary processes considered for the calculation of the effective ionization coefficient. The corresponding rate coefficients are averaged over the values given in the stated references, and have units of $cm^3\ s^{-1}$ for two-body reactions and $cm^6\ s^{-1}$ for three-body reactions.

Reaction	Rate coeff.	Reference
$He + e^- \xrightarrow{k_i} He^+ + 2e^-$	$f(E/n)$	[28]
$He + e^- \xrightarrow{k_m} He^m + e^-$	$f(E/n)$	[28]
$He^m + 2He \xrightarrow{k_c} He_2^m + He$	1.8×10^{-34}	[30–32]
$He^m + N_2 \xrightarrow{k_p^1} He + N_2^+ + e^-$	6.75×10^{-11}	[33–36]
$He^m + N_2 + He \xrightarrow{k_p^2} 2He + N_2^+ + e^-$	3.5×10^{-30}	[34–36]
$He^m + O_2 \xrightarrow{k_p^3} He + O_2^+ + e^-$	2.5×10^{-10}	[35, 37–39]
$He^m + O_2 + He \xrightarrow{k_p^4} 2He + O_2^+ + e^-$	4.2×10^{-30}	[35, 38]
$He_2^m + N_2 \xrightarrow{k_p^5} 2He + N_2^+ + e^-$	5×10^{-10}	[20, 35]
$He_2^m + O_2 \xrightarrow{k_p^6} 2He + O_2^+ + e^-$	4.5×10^{-10}	[35, 40]

just as done in [24, 25]. Here, g denotes the discharge gap width and $\alpha_{\mathrm{eff}}(E/n)$ is the effective ionization coefficient. In general, $\alpha_{\mathrm{eff}}(E/n)$ depends on the axial distribution of the reduced electric field strength E/n. However, the breakdown voltage is reached at least about 10 μs before the discharge current maximum, see figure 8, and thus still within the late Townsend pre-phase of the glow-like BD. This phase is characterized by a gradual increase in the charge carrier density resulting in a low 'starting current'. Hence, there is still no significant space charge formation, wherefore the electric field and thus $\alpha_{\mathrm{eff}}(E/n)$ are approximated to be constant across the discharge gap when the breakdown voltage U_b is reached. As a consequence, the ionization integral in equation (9) results in $\alpha_{\mathrm{eff}}(U_b) \times g$. Later on, the electric field gets strongly disturbed during the propagation of the cathode-directed ionization front, as shown for similar discharge conditions in [17].

The effective ionization coefficient α_{eff} is calculated from the ratio between the effective ionization rate r_{eff} and the electron drift velocity v_e^d,

$$\alpha_{\mathrm{eff}}(E/n) = \frac{r_{\mathrm{eff}}(E/n)}{v_e^d(E/n)} = \frac{k_{\mathrm{eff}}(E/n)}{\mu_e(E/n)E/n}. \tag{10}$$

Here, k_{eff} is the effective rate coefficient including all relevant ionization processes, and μ_e is the electron mobility. The considered elementary processes are listed in table 2. For moderate reduced electric field strength, both the direct electron impact ionization (k_i), resulting in Townsend's first ionization coefficient, and the electron impact excitation of atomic (k_m) and molecular (k_c) helium metastable states, followed by Penning ionization of always present gas impurities ($k_p^1 - k_p^6$), contribute to the effective ionization.

The rate coefficients for the electron impact ionization from the He ground state and electron impact excitation of atomic helium metastable states are functions of the reduced electric field strength E/n and are calculated with BOLSIG+ [26–29]. The rate coefficients for conversion of the metastable atom He^m to the metastable molecule He_2^m, and for Penning ionization are mean values from the stated references. The rate coefficients for two-body and three-body Penning ionization of impurities $M = \{N_2, O_2\}$ by metastable He atoms are summed up pairwise (the background gas density $[He] = p/(k_B T_g)$ was canceled out in three-body reactions), resulting in the composite rate coefficients k_p^{1+2} and k_p^{3+4}. Furthermore, the gas impurities are treated as synthetic air defined by the density ratio $[N_2]/[O_2] = 4/1$, yielding the effective rate coefficients for Penning ionization $k_p^{1-4} = (4/5\, k_p^{1+2} + 1/5\, k_p^{3+4})$ by He^m, and $k_p^{5+6} = (4/5\, k_p^5 + 1/5\, k_p^6)$ by He_2^m.

Finally, for fixed values of the reduced electric field strength and the impurity concentration, the density ratio $R_m = [He_2^m]/[He^m]$ becomes constant after a short time. First, the introduction of R_m allows the analytical solution of the rate equation system based on the elementary processes in table 2. Second, the kinetics of He_2^m are not reasonably described by this reduced set of considered reactions. But, as pointed out by a fluid simulation for quite similar discharge conditions [17], the He_2^m density remains approximately one order of magnitude lower than the He^m density during the overall discharge duration. The density ratio R_m is nevertheless considered as a (temporally constant) parameter and its influence on the effective SEE coefficient is shown at the end of this section. Summarized, the rate equation system simplifies to

$$\begin{aligned}\frac{d[He^m]}{dt} &= k_m[He][e^-] - (k_p^{1-4}[M] + k_c[He]^2)[He^m] \\ &\equiv c_m[e^-] - (c_p^{1-4} + c_c)[He^m],\end{aligned} \tag{11}$$

$$\begin{aligned}\frac{d[e^-]}{dt} &= k_i[He][e^-] + k_p^{1-4}[M][He^m] + k_p^{5+6}[M][He_2^m] \\ &\equiv c_i[e^-] + (c_p^{1-4} + c_p^{5+6}R_m)[He^m],\end{aligned} \tag{12}$$

and can be separated resulting in a differential equation for the electron density only,

$$\begin{aligned}0 = \frac{d^2[e^-]}{dt^2} + \underbrace{(c_c + c_p^{1-4} - c_i)}_{a}\frac{d[e^-]}{dt} \\ \underbrace{-(c_i(c_c + c_p^{1-4}) + c_m(c_p^{1-4} + c_p^{5+6}R_m))}_{b}[e^-].\end{aligned} \tag{13}$$

Inserting the exponential approach $[e^-](t) = A\exp(\omega t)$ into the differential equation (13) yields a quadratic equation with two real solutions

$$\omega_{1,2} = \frac{a}{2}\left(\pm\sqrt{1 + 4\frac{b}{a^2}} - 1\right). \tag{14}$$

Already after some tens of nanoseconds, which is short compared to the microsecond time scale of the diffuse BD, the general solution for the electron density in equation (14) equals the continuous exponential rise according to $A\exp(\omega t)$, with $\omega > 0$, wherefore the negative solution $\omega < 0$ can be neglected. For small impurity concentrations $[M]/[He] \leqslant 10^{-3}$ just as in the present experiment, and for values of the reduced electric field larger than about 5 Td, the rates for the excitation of

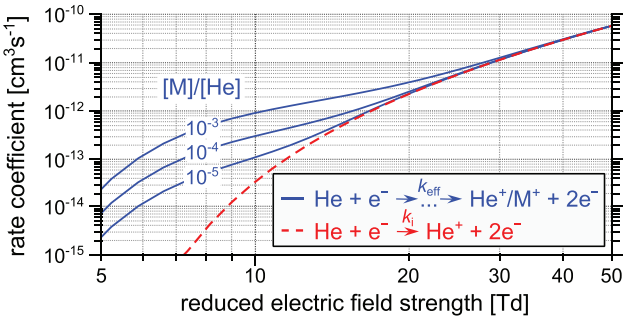

Figure 9. Rate coefficients for direct electron impact ionization of He (dashed red line), calculated with BOLSIG+ [26, 27, 29], and for the overall effective ionization (blue lines) according to equation (16) as a function of the reduced electric field strength. Gas temperature $T_g = 350$ K, air impurities $[N_2]/[O_2] = 4/1$, metastables density ratio $[He_2^m]/[He^m] = 1/10$.

He metastable atoms (c_m) and electron impact ionization (c_i) significantly exceed the rates for metastable's conversion (c_c) and Penning ionization (c_p^{1-4}, c_p^{5+6}). Here, the positive solution simplifies to

$$\omega \approx \frac{c_i}{2}\left(\sqrt{1+4\frac{c_p^{1-4}(c_m+c_i)}{c_i^2}}+1\right). \qquad (15)$$

Inserting this solution in the rate equation for effective electron multiplication, according to the rate coefficient k_{eff} for effective ionization,

$$\frac{d[e^-]}{dt} = \omega[e^-] = k_{eff}[He][e^-], \qquad (16)$$

and comparison of the coefficients yields $k_{eff} = \omega/[He]$. In figure 9, the rate coefficient k_{eff} for effective ionization is plotted as a function of the reduced electric field strength for different impurity concentrations [M]/[He], together with the rate coefficient k_i for electron impact ionization from the He ground state. For reasonable impurity concentrations, k_{eff} exceeds k_i for values of E/n lower than 30 Td. This range includes the electric field strength $E_b = U_b/g$ that is necessary for the discharge breakdown under the experimental conditions studied. Therefore, Penning ionization must be considered in the calculations even for very low impurity levels.

With $k_{eff}(E_b)$ and the electron mobility $\mu_e(E_b)$ taken from BOLSIG+, the effective ionization coefficient $\alpha_{eff}(E_b)$ is calculated with equation (10). Finally, the effective SEE coefficients $\gamma_{eff}(E_b)$ for the different dielectrics are estimated using Townsend's criterion in equation (9). Figure 10 plots the SEE coefficients in dependence of uncertain quantities which are included in the analytical calculations: (a) air impurity concentration [M]/[He], (b) metastable density ratio $[He_2^m]/[He^m]$, (c) discharge diameter in lateral direction and (d) gas temperature. Regarding the variation of the air impurity level, reasonable values lie between 50 ppm and 200 ppm resulting in a relative deviation of about 30% in γ_{eff}. As well, the calculation of γ_{eff} depends crucially on the discharge diameter that determines the breakdown voltage U_b calculated from measured electrical quantities according to equation (1). Estimating the discharge diameter from the surface charge measurements is

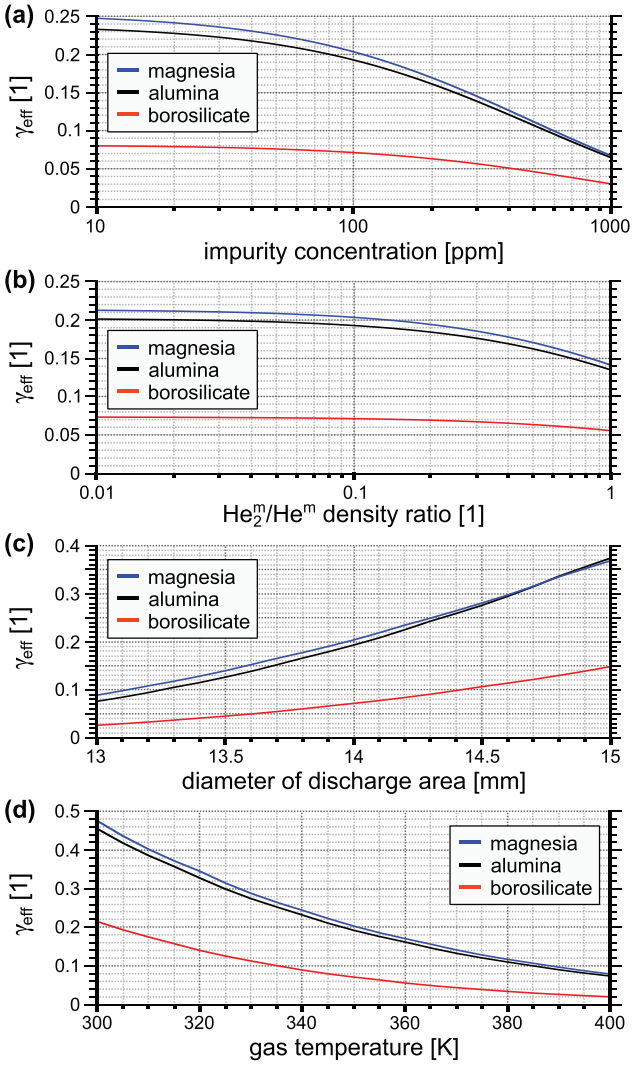

Figure 10. Effective SEE coefficient γ_{eff} for borosilicate glass, alumina and magnesia depending on (a) the air impurity ratio [M]/[He], (b) the density ratio of metastable states $[He_2^m]/[He^m]$, (c) the lateral discharge extent and (d) the gas temperature. Otherwise, the parameters are fixed to [M]/[He] = 100 ppm, $[He_2^m]/[He^m] = 1/10$, $d_{dis} = 14$ mm, and $T_g = 350$ K.

difficult, because the incident charge carriers from the discharge volume get distracted in a lateral direction due to the already deposited charge of same polarity. Though, from the steep slope of the $Q_{ext}(U_{ext})$ plot (Lissajous figure), one can estimate a discharge diameter of about 14 mm. However, the ratio $[He_2^m]/[He^m]$ has no remarkable influence. Besides, a reliable value of about $[He_2^m]/[He^m] \sim 0.1$ is given by a fluid simulation for similar discharge conditions [17]. The gas temperature T_g defines the background gas density $n = p/(k_b T_g)$, and thus determines the reduced electric field strength E_b/n required for discharge breakdown, as well as all reaction rates included in the calculation of α_{eff} by equation (10).

In spite of these uncertain parameters, the values obtained for the effective SEE coefficients, considering SEE by ions and photons as well as thermal desorption, lie between 0.02 and 0.4 for the different dielectrics. Especially, values of γ_{eff} for magnesia and alumina even close to one were reported in [24, 25] using Townsend's criterion as well. According

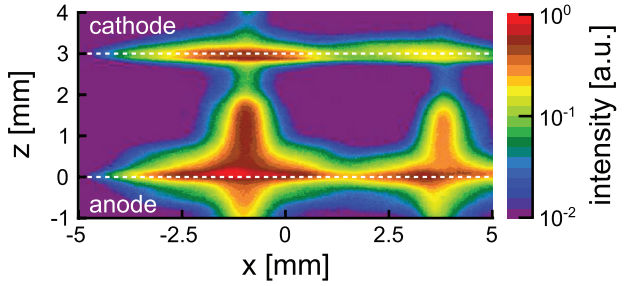

Figure 11. ICCD camera image of the optical emission averaged over the breakdown duration of two self-stabilized discharge filaments. Borosilcate glass on top of the BSO crystal, helium with 10% nitrogen admixture, $p = 1$ bar, $\hat{U}_{ext} = 2.3$ kV.

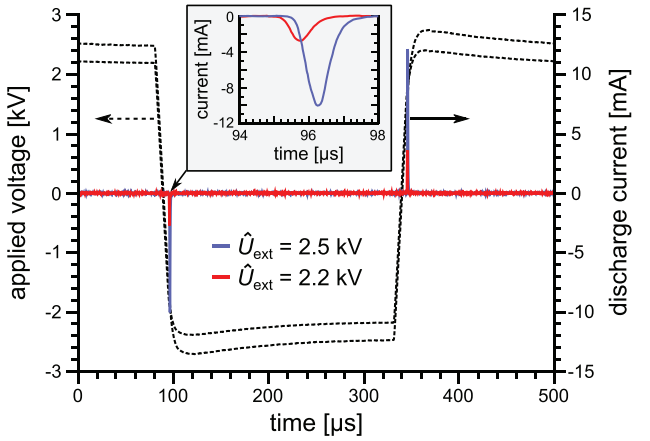

Figure 12. Square-wave feeding voltage and discharge current over one discharge cycle for two different voltage amplitudes $\hat{U}_{ext} = 2.5$ kV (four filaments) and $\hat{U}_{ext} = 2.2$ kV (one single filament). Borosilcate glass on top of the BSO crystal, helium with 10% nitrogen admixture, $p = 1$ bar.

to the simulation in [17], SEE by N_2^+ and O_2^+ impurity ions dominates by one order of magnitude over SEE by photons and thermal desorption during the breakdown. Hence, the obtained values for γ_{eff} could be related to SEE by ion impact.

4. Self-stabilized discharge filaments

4.1. Discharge characteristics

Self-stabilized discharge filaments were operated with a square-wave feeding voltage in helium with 10 vol.% nitrogen admixture at a pressure of 1 bar. Exemplary, figure 11 shows an ICCD camera image of the optical emission averaged over the breakdown duration of two self-stabilized discharge filaments. The characteristics are partly reminiscent of the glow-like BD in helium [5] and the microdischarge (MD) regime that is typically observed in air [41]. Two localized emission maximums in front of both dielectrics indicate the negative and positive glow; near to the cathode there is a Faraday dark space followed by a (kind of) positive column, and surface discharges propagate in a radial direction on both dielectrics. The time-resolved measurements reveal also a Townsend pre-phase of microsecond duration with weak emission maximum in front of the anodic dielectric, followed by the fast cathode-directed ionization front on the nanosecond time scale. However, as can be seen from the discharge current in figure 12, the overall discharge duration is on the microsecond time scale, and thus comparable to laterally patterned BDs typically operated at lower pressures and discharge gap widths smaller than 1 mm [9, 10]. Moreover, several discharge filaments appear almost simultaneously, as also found in patterned BDs. This is shown by the current of four discharge filaments driven by $\hat{U}_{ext} = 2.5$ kV (blue lines) compared to a single discharge filament at $\hat{U}_{ext} = 2.2$ kV (red lines).

4.2. Spatial conservation of discharge filaments

In this section, the focus is on the importance of the surface charge distribution for the spatial conservation of discharge filaments in the plane-parallel electrode configuration. In practice, operating the self-stabilized discharge filaments is achieved by reducing the feeding voltage amplitude after the discharge ignition in the microdischarge regime. Figure 13 shows this procedure. Here, the surface charge density spots (averaged over some discharge cycles) represent the 'footprints' of the discharge filaments, starting with arbitrary distributed MDs for $\hat{U}_{ext} = 3.2$ kV, followed by rotating and then stable filament patterns between 3.0 kV and 2.3 kV, and ending up with a single stable discharge filament for 2.2 kV. Again, the possibility to operate a single discharge filament might be explained by inhomogeneities in the discharge gap width and the gas flow rate. It is striking that the surface charge spots can differ from a circular profile which depends on the respective pattern and is most notable at 2.4 kV. The incident charge carriers of the same polarity get laterally distracted, both during the breakdown and the subsequent surface discharge, which can deform the final surface charge distribution. Due to the long lifetime of surface charges, this deformation influences the following discharge breakdown and thus the spatial long-term stability. Here, two discharge filaments and a single one turned out to be the most stable systems.

The mechanism behind the mode transition from arbitrary distributed MDs to stable filament patterns (and vice versa) is associated with the spatio-temporal evolution of the gap voltage. The latter is calculated by equation (7) from the measured surface charge density. In figure 14(a), the spatial distribution of the gap voltage is depicted just before the breakdown of four discharge filaments ($\hat{U}_{ext} = 2.5$ kV) and a single filament ($\hat{U}_{ext} = 2.2$ kV) during the negative half-cycle of the feeding voltage. The electric field caused by residual surface charges contributes significantly to the gap voltage: at the edges, where no surface charges were accumulated, the gap voltage is only -1.6 kV equal to the partial feeding voltage drop across the gas gap, whereas the required breakdown voltage of about -2.6 kV is only reached at the center of the surface charge spots. Thus the additional electric field caused by the surface charge spot enhances the gap voltage by about -1 kV with respect to the partial feeding voltage drop. This result emphasizes the outstanding importance of the spatial surface charge distribution for the self-stabilization of discharge filaments (surface memory effect). Besides, metastable species (and even charge carriers in regions with low electric

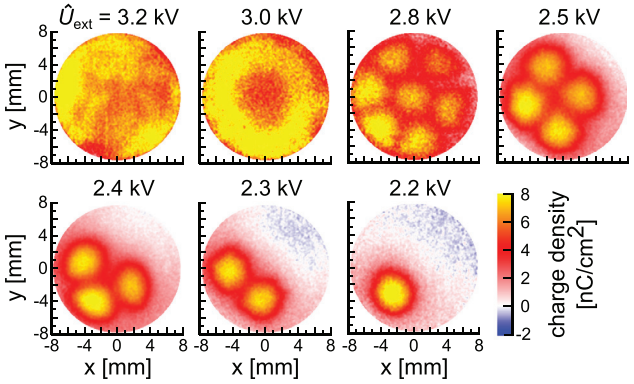

Figure 13. Spatial distribution of the surface charge density after the filamentary breakdown within the positive half-cycle of the discharge for different feeding voltage amplitudes. Borosilcate glass on top of the BSO crystal, helium with 10% nitrogen admixture, $p = 1$ bar.

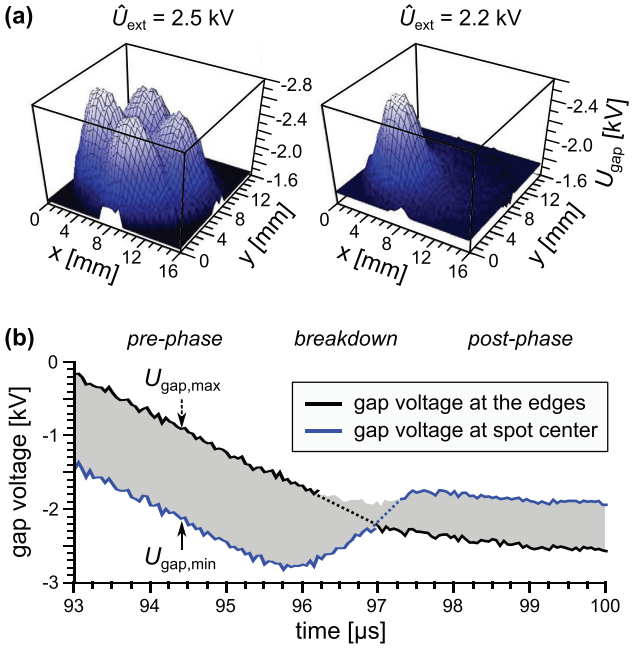

Figure 14. Spatio-temporally resolved gap voltage during the formation of self-stabilized discharge filaments: (a) spatial gap voltage distribution just before the discharge breakdown in the negative half-cycle of the discharge for two different voltage amplitudes and (b) dynamics of the minimum and maximum gap voltage for $\hat{U}_{ext} = 2.5$ kV, from the discharge pre-phase to the post-phase. Borosilcate glass on top of the BSO crystal, helium with 10% nitrogen admixture, $p = 1$ bar.

field) might survive during two consecutive discharge breakdowns (volume memory effect) and contribute to the pre-ionization and thereby to the local re-ignition of the discharge filaments.

In figure 14(b), the maximum and the minimum of the gap voltage distribution are plotted as time-resolved for the case of the four discharge filaments at $\hat{U}_{ext} = 2.5$ kV feeding voltage amplitude, compared to figure 14(a). Thus, the gray colored area encloses the whole gap voltage range over the entire electrode area, whereas the black and blue curves indicate the temporal development of the gap voltage at the edges and in

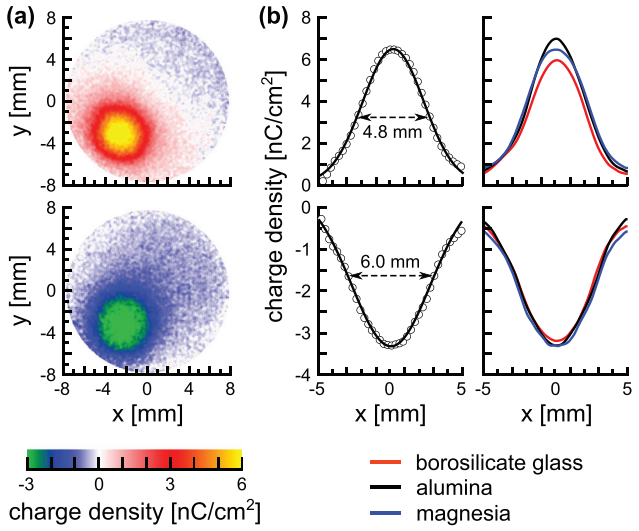

Figure 15. Positive and negative surface charge spots as the footprints of a single self-stabilized discharge filament: (a) 2D surface charge density distributions and (b) corresponding 1D profiles through the maximum and minimum, respectively, for different dielectrics on top of the BSO crystal. Helium with 10% nitrogen admixture, $p = 1$ bar, $\hat{U}_{ext} = 2.2$ kV.

the center of the surface charge spots, respectively. Regarding the spot centers, the gap voltage drops significantly after the breakdown voltage was reached. In contrast, the required breakdown voltage is never reached in the surrounding regions, wherefore no additional discharge events occur after the initial simultaneous ones. However, the discharge stability get lost when the feeding voltage amplitude is continually increased. The breakdown voltage is then reached also outside the spot centers which first causes rotating filament patterns and, finally at significant over-voltage, the transition to the microdischarge regime.

4.3. Influence of different dielectrics

In figure 15(a), the surface charge density distribution for a single self-stabilized discharge filament as well as (b) the 1D radial profiles through the center of the positive and negative surface charge spots are plotted in comparison for the three dielectrics studied. Both the positive and negative surface charge profiles can be approximated by a Gaussian distribution with height $\sigma_{p,n}$ and full width at half maximum $w_{p,n}$, as already shown in previous investigations on the mere BSO crystal [7, 8]. The positive surface charge density profile peaks at about 6 nC cm^{-2} which is twice as large as the height of the negative profile, -3 nC cm^{-2}. Although, conversely, w_n is larger than w_p, however, the overall amount of deposited charge

$$Q_{p,n} \approx \frac{\pi}{2} w_{p,n}^2 \sigma_{p,n} \tag{17}$$

is clearly larger for the positive polarity ($Q_p \approx 2.2$ nC) than for the negative polarity ($Q_n \approx -1.7$ nC). This discrepancy may indicate the recombination of surface electrons with positive ions stored in a region with low electric field during the discharge afterglow. But note that a mismatch between the

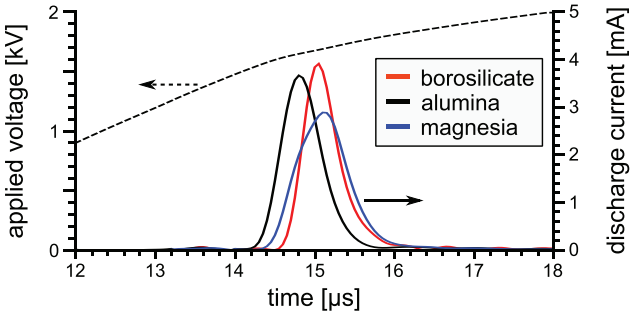

Figure 16. Discharge current of a single self-stabilized discharge filament for different materials acting as the cathodic dielectric. Helium with 10% nitrogen admixture, $p = 1$ bar, $\hat{U}_{\mathrm{ext}} = 2.2$ kV.

overall amounts of positive and negative surface charges was also observed for the microdischarge regime in [7, 8].

The comparison between the negative and positive surface charge density profiles for the three dielectrics reveals no remarkable difference in the full width at half maximum, but in the overall amount of deposited surface charge. This is particularly true for the positive polarity, as shown on the right side of figure 15(b). As reported in [11], the lateral diffusion of surface charges on the dielectrics occurs on the second time scale and hence has no influence on the dimensions of the surface charge profiles during the discharge operation. But, as already discussed for the diffuse BD, the amount of surface charges is influenced by the permittivity. The latter is largest for alumina ($\varepsilon_{\mathrm{r}} = 10.55$), closely followed by magnesia ($\varepsilon_{\mathrm{r}} = 9.65$), and clearly smallest for borosilicate glass ($\varepsilon_{\mathrm{r}} = 6.7$), which agrees with the ranking of the measured surface charge amount.

In figure 16, the discharge current is plotted for a single discharge filament operated at $\hat{U}_{\mathrm{ext}} = 2.2$ kV comparing the three materials acting as the cathodic dielectric. The discrepancy in the breakdown onset with respect to the feeding voltage can be explained by two different aspects. First, the breakdown voltage is largest for borosilicate glass (2.715(16) kV), followed by alumina (2.665(14) kV) and smallest for magnesia (2.600(14) kV). The cathodic dielectric material also has a crucial influence on the filamentary discharge, due to secondary electron emission during the Townsend pre-phase, as discussed for the diffuse BD in section 3. Consequently, the effective SEE coefficient is largest for magnesia, in agreement with the results for the diffuse discharge. The SEE yield influences the formation of a critical space charge that initiates the cathode-directed ionization front and thus the breakdown onset. Second, the electrostatic memory effect depends on the overall amount of deposited surface charges that is largest for alumina, as shown in figure 15(b). Summarized, the breakdown condition is at first reached for alumina, second for magnesia and at last for borosilicate glass.

5. Summary and outlook

The presented work reports on the successful extension of the surface charge diagnostics based on the electro-optic Pockels effect of a bismuth silicon oxide (BSO) crystal to more commonly used dielectric materials in barrier discharge configurations. This was achieved by covering the BSO crystal with a variable transparent dielectric such as borosilicate glass, alumina and magnesia. The applicability is proved by the excellent agreement of the phase-resolved surface charge with the overall transported charge during the operation of the homogeneous glow-like BD. Beyond, the measuring accuracy of the advanced surface charge diagnostics is once more enhanced in comparison to previous works.

The combination and correlation of this method with the measurement of electrical characteristics and ICCD camera imaging was performed on the diffuse glow-like BD in nominally pure helium at 500 mbar, and the self-stabilized filamentary discharge in helium with 10 vol.% nitrogen admixture at 1 bar. Regarding the diffuse glow-like BD, a significant discrepancy in the breakdown voltage is caused by variation of the cathodic dielectric material, due to different secondary electron emission (SEE) coefficients. In particular, the results indicate that magnesia has the largest effective SEE coefficient. This was also quantified using Townsend's criterion for the breakdown voltage in combination with analytical calculations of the effective ionization coefficient in helium with small air impurities. In spite of the uncertainties, e.g. in the gas impurity concentration, gas temperature and lateral discharge extent, reasonable values for the effective SEE coefficients between 0.02 and 0.4 were obtained from this approach for the different dielectrics studied.

The crucial impact of the surface charge memory effect on the re-ignition behavior was demonstrated for the filamentary discharge. Single discharge filaments operated in the plane-parallel electrode configuration can periodically reignite at the same positions due to the long lifetime of surface charges, which are Gaussian distributed in local spots marking the 'footprints' of the discharge filaments. The transition to arbitrary distributed microdischarges is avoided and in turn the discharge filaments are spatially conserved as long as the breakdown voltage is only reached at the center of the surface charge spots. This was concluded from the spatio-temporal evolution of the gap voltage. Just as pointed out for the diffuse discharge, the influence of different dielectrics on the filamentary discharge is observable in the amount of deposited surface charge that increases with rising permittivity, as well as in the pre-ionization during the Townsend pre-phase, which depends on the effective SEE yield.

In order to improve the estimation of effective SEE coefficients using Townsend's criterion for the breakdown voltage, the investigation of the diffuse Townsend-like BD in nitrogen is favorable, due to the approximately constant electric field across the gas gap during the whole breakdown duration. However, the discharge operation in nitrogen demands high-power supplies and small discharge gap widths, respectively. Moreover, the comprehensive study of the existence regimes, stability criteria (volume and surface memory effect) and breakdown mechanism of the single self-stabilized discharge filament by combined volume and surface diagnostics is planned as well.

Acknowledgments

The presented work was supported by the Deutsche Forschungsgemeinschaft through the Project No. B11 of the Transregional Collaborative Research Center 24 (TRR 24), 'Fundamentals of Complex Plasmas'.

References

[1] Kogelschatz U 2003 Dielectric-barrier discharges: their history, discharge physics, and industrial applications *Plasma Chem. Plasma Process.* **23** 1–46
[2] Becker K H, Kogelschatz U, Schoenbach K H and Barker R J 2004 *Non-Equilibrium Air Plasmas at Atmospheric Pressure* (*Series in Plasma Physics*) (Bristol: Institute of Physics Publishing)
[3] Wagner H-E, Brandenburg R, Kozlov K V, Sonnenfeld A, Michel P and Behnke J F 2003 The barrier discharge: basic properties and applications to surface treatment *Vacuum* **71** 417–36
[4] Fridman G, Friedman G, Gutsol A, Shekhter A B, Vasilets V N and Fridman A 2008 Applied plasma medicine *Plasma Process. Polym.* **5** 503–33
[5] Massines F, Gherardi N, Naudé N and Ségur P 2009 Recent advances in the understanding of homogeneous dielectric barrier discharges *Eur. Phys. J. Appl. Phys.* **47** 22805
[6] Kogelschatz U 2010 Collective phenomena in volume and surface barrier discharges *J. Phys.: Conf. Ser.* **257** 012015
[7] Bogaczyk M, Wild R, Stollenwerk L and Wagner H-E 2012 Surface charge accumulation and discharge development in diffuse and filamentary barrier discharges operating in He, N_2 and mixtures *J. Phys. D: Appl. Phys.* **45** 465202
[8] Tschiersch R, Bogaczyk M and Wagner H-E 2014 Systematic investigation of the barrier discharge operation in helium, nitrogen, and mixtures: discharge development, formation and decay of surface charges *J. Phys. D: Appl. Phys.* **47** 365204
[9] Stollenwerk L, Laven J G and Purwins H-G 2007 Spatially resolved surface-charge measurement in a planar dielectric-barrier discharge system *Phys. Rev. Lett.* **98** 255001
[10] Wild R and Stollenwerk L 2014 Phase-resolved measurement of the spatial surface charge distribution in a laterally patterned barrier discharge *New J. Phys.* **16** 113040
[11] Wild R, Benduhn J and Stollenwerk L 2014 Surface charge transport and decay in dielectric barrier discharges *J. Phys. D: Appl. Phys.* **47** 435204
[12] Golubovskii Yu B, Maiorov V A, Behnke J and Behnke J F 2002 Influence of interaction between charged particles and dielectric surface over a homogeneous barrier discharge in nitrogen *J. Phys. D: Appl. Phys.* **35** 751–61
[13] Li M, Li C, Zhan H and Xu J 2008 Effect of surface charge trapping on dielectric barrier discharge *Appl. Phys. Lett.* **92** 031503
[14] Ambrico P F, Ambrico M, Colaianni A, Schiavulli L, Dilecce G and De Benedictis S 2010 Thermoluminescence study of the trapped charge at alumina surface electrode in different dielectric barrier discharges regimes *J. Phys. D: Appl. Phys.* **43** 325201
[15] Heinisch R L, Bronold F X and Fehske H 2012 Electron surface layer at the interface of a plasma and a dielectric wall *Phys. Rev.* B **85** 075323
[16] Naudé N, Belinger A, Dap S and Gherardi N 2015 Memory effects in Atmospheric Pressure Townsend Discharges in N_2 and air *Proc. 32nd Int. Conf. on Phenomena in Ionized Gases (Iasi, 2015)*
[17] Nemschokmichal S, Tschiersch R and Meichsner J 2016 The influence of negative ions in helium-oxygen barrier discharges: II 1D numerical simulation and adaption to the experiment *Plasma Sources Sci. Technol.* **25** 055024
[18] Nemschokmichal S and Meichsner J 2015 Spatio-temporal characterization of $N_2(A^3\Sigma_u^+)$ metastables in diffuse nitrogen barrier discharge *J. Phys. D: Appl. Phys.* **48** 405203
[19] Tschiersch R, Nemschokmichal S and Meichsner J 2016 The influence of negative ions in helium-oxygen barrier discharges: I. Laser photodetachment experiment *Plasma Sources Sci. Technol.* **25** 025004
[20] Golubovskii Yu B, Maiorov V A, Behnke J and Behnke J F 2003 Modelling of the homogeneous barrier discharge in helium at atmospheric pressure *J. Phys. D: Appl. Phys.* **36** 39–49
[21] Guaitella O, Marinov I and Rousseau A 2011 Role of charge photodesorption in self-synchronized breakdown of surface streamers in air at atmospheric pressure *Appl. Phys. Lett.* **98** 071502
[22] Marbach J, Bronold F X and Fehske H 2012 Resonant charge transfer at dielectric surfaces *Eur. Phys. J.* D **66** 106
[23] Golubovskii Yu B, Maiorov V A, Li P and Lindmayer M 2006 Effect of the barrier material in a Townsend barrier discharge in nitrogen at atmospheric pressure *J. Phys. D: Appl. Phys.* **39** 1574–83
[24] Suzuki S and Itoh H 2014 Secondary ionization coefficient γ of MgO, SrO and CaO and the correlation between γ and charge accumulated on CaO in argon *Plasma Sources Sci. Technol.* **23** 065030
[25] Suzuki S and Itoh H 2015 Gradual increase in secondary ionization coefficient γ and charge accumulation on a dielectric electrode during DBD with repeated breakdown *Plasma Sources Sci. Technol.* **24** 055016
[26] Hagelaar G J M and Pitchford L C 2005 Solving the Boltzmann equation to obtain electron transport coefficients and rate coefficients for fluid models *Plasma Sources Sci. Technol.* **14** 722–33
[27] LXCat, www.lxcat.laplace.univ-tlse.fr, retrieved April 2016
[28] Lisbon database, www.lxcat.net, retrieved April 2016
[29] Phelps database, www.lxcat.laplace.univ-tlse.fr, retrieved April 2016
[30] Phelps A V and Molnar J P 1953 Lifetimes of metastable states of noble gases *Phys. Rev.* **82** 1202
[31] Deloche R, Monchicourt P, Cheret M and Lambert F 1976 High-pressure helium afterglow at room temperature *Phys. Rev.* A **13** 1140–76
[32] Emmert F, Angermann H H, Dux R and Langhoff H 1988 *J. Phys. D: Appl. Phys.* **21** 667
[33] Smirnov B M 1974 *Ions and Excited Atoms in Plasma* (Moscow: Atomizdat) (in Russia)
[34] Lee F W and Collins C B 1976 Measurement of the rate coefficients for the bimolecular and termolecular deexcitation reactions of $He(2^3S)$ with Ne, Ar, N_2, CO, CO_2, and CH_4^* *J. Chem. Phys.* **65** 5189–97
[35] Myers G and Cunningham A J 1977 Quenching reactions of $He(2^3S)$ and $He_2(2^3\Sigma)$ metastables in the presence of N_2 and O_2 *J. Chem. Phys.* **67** 3352–59
[36] Pouvesle J M, Bouchole A and Stevefelt J 1982 Modeling of the charge transfer afterglow excited by intense electrical discharges in high pressure helium nitrogen mixtures *J. Chem. Phys.* **77** 817
[37] Lindinger W, Schmeltekopf A L and Fehsenfeld F C 1974 Temperature dependence of de-excitation rate constants of $He(2^3S)$ by Ne, Ar, Xe, H_2, N_2, O_2, NH_3, and CO_2 *J. Chem. Phys.* **61** 2890–95

[38] Pouvesle J M, Khacef A, Stevefelt J, Jahani H, Gylys V T and Collins C B 1988 Study of two-body and three-body channels for the reaction of metastable helium atoms with selected atomic and molecular species *J. Chem Phys.* **88** 3061–71

[39] Stafford D S and Kushner M J 2004 $O_2(^1\Delta)$ production in He/O_2 mixtures in flowing low pressure plasmas *J. Appl. Phys.* **96** 2451

[40] Pouvesle J M and Stevefelt J 1985 Reactivity of metastable helium molecules in atmospheric pressure afterglows *J. Chem. Phys.* **83** 2836

[41] Kozlov K V, Wagner H-E, Brandenburg R and Michel P 2001 Spatio-temporally resolved spectroscopic diagnostics of the barrier discharge in air at atmospheric pressure *J. Phys. D: Appl. Phys.* **34** 3164–76